Solid-state NMR of Spin-9/2 Nuclei ^{115}In and ^{209}Bi in Functional Inorganic Complex Oxides

Kent J. Griffith[*], Fenghua Ding, Steven Flynn

Department of Chemistry, Northwestern University, 2145 Sheridan Road, Evanston, IL 60208

Abstract

Indium and bismuth are technologically important elements, in particular as oxides for optoelectronic applications. ^{115}In and ^{209}Bi are both $I = 9/2$ nuclei with high natural abundances and moderately high frequencies but large nuclear electric quadrupole moments. Leveraging the quadrupolar interaction as a measure of local symmetry and polyhedral distortions for these nuclei could provide powerful insights on a range of applied materials. However, the absence of reported NMR parameters on these nuclei, particularly in oxides, hinders their use by the broader materials community. In this contribution, solid-state ^{115}In and ^{209}Bi NMR of three recently discovered quaternary bismuth or indium oxides are reported, supported by density functional theory calculations, numerical simulations, diffraction, and additional multinuclear (^{27}Al, ^{69,71}Ga, ^{121}Sb) solid-state NMR measurements. The compounds $LiIn_2SbO_6$, $BiAlTeO_6$, and $BiGaTeO_6$ are measured without special equipment at 9.4 T, demonstrating that wideline techniques such as the QCPMG pulse sequence and frequency-stepped acquisition can enable straightforward extraction of quadrupolar tensor information in $I = 9/2$ ^{115}In and ^{209}Bi even in sites with large quadrupolar coupling constants. Relationships are described between the NMR observables and local site symmetry. These are amongst the first reports of the NMR parameters of ^{115}In, ^{121}Sb, and ^{209}Bi in oxides.

Introduction

Bismuth- and indium-based complex oxides, *i.e.,* oxides containing multiple metal cations, are important functional inorganic materials with a central role in many optoelectronic and energy-related applications. Tin-doped bixbyite indium oxide (In_2O_3) is an n-type transparent conducting oxide[1–3] used in display technology,[4,5] electrochromic smart windows,[6–8] and photovoltaics[9–11]. Complex indium-containing oxides are being developed for the next generation of electronic materials.[12–16] Lithium indium oxides have been studied as prospective solid electrolytes for all-solid-state lithium-ion batteries.[17–19] Substituted versions of fluorite bismuth oxide (δ-Bi_2O_3)[20–23] and Aurivillius-type mixed-metal bismuth oxides [20,24,25] host some of the highest known high oxygen-ion conductivities. Bismuthate glasses are non-toxic candidates to replace lead oxide in zero-stress optic materials.[26,27] The stereochemically active lone pair in Bi^{3+} can lead to noncentrosymmetric structures with useful optoelectronic and ferroic properties.[28–32]

Given the range of technological applications and frequently cation-mixed and/or poorly diffracting nature of bismuth and indium oxides, it is desirable to develop alternative metrologies to study their atomic environments. ^{115}In and ^{209}Bi solid-state nuclear magnetic resonance (NMR) spectroscopy could, in principle, offer additional insights into the local coordination, symmetry, and ionic/polyhedral dynamics. The quadrupolar interaction, specifically, yields information on the spherical (C_Q) and axial (η_Q) symmetry.[33] Both nuclei are spin 9/2 with moderate gyromagnetic ratios ($\gamma_{^{115}In}$ = 5.8972 $\times$ 10^7 rad s^{-1} T^{-1}; $\gamma_{^{209}Bi}$ = 4.3750 $\times$ 10^7 rad s^{-1} T^{-1}), large nuclear electric quadrupole moments ($Q_{^{115}In}$ = 77.2(5) fm^2; $Q_{^{209}Bi}$ = –51.6(2) fm^2), and high natural abundances (^{115}In = 95.71%; ^{209}Bi = 100%).[34,35] Note that ^{113}In is also spin 9/2 with nearly identical nuclear properties ($\gamma_{^{113}In}$ = 5.8845 $\times$ 10^7 rad s^{-1} T^{-1}; $Q_{^{113}In}$ = 76.1(5) fm^2); however, it comprises only 4.29% natural abundance and is thus

disfavored. An analogy must be drawn to ^{93}Nb, the only other stable, odd-proton $I = 9/2$ nucleus (*nota bene,* there are several odd-neutron $I = 9/2$ nuclides—^{73}Ge, ^{83}Kr, ^{87}Sr, and ^{179}Hf —but these have substantially lower gyromagnetic ratios). ^{93}Nb has found wider use than its $^{(113)/115}$In and ^{209}Bi counterparts, primarily owing to its smaller nuclear quadrupole moment ($Q_{^{93}Nb} = -32(2)$ fm^2). Combined with its slightly higher frequency ($\square_{^{93}Nb} = 6.5674 \times 10^7$ rad s^{-1} T^{-1}) and 100% natural abundance, ^{93}Nb has been used to provide insights on a wide range of materials.[36–41]

Owing to quadrupolar broadening, ^{115}In and ^{209}Bi NMR studies are infrequent. Both nuclei have been studied in a number of halide systems[42–49] and molecular compounds[48–53]. Reports on oxides are exceedingly rare. A pair of very recent reports suggests growing interest in this area.[16,54] Yamada *et al.* carried out field-swept ^{115}In NMR to determine the quadrupolar coupling parameters of the two indium sites in In$_2$O$_3$,[54] complementing the values determined via nuclear quadrupolar resonance (NQR) spectroscopy in the literature;[55] chemical shift information was not determined. Huang *et al.* employed ^{115}In NMR to study amorphous indium gallium oxide processed with varying polyvinyl alcohol contents. In the latter study, a distinct ^{115}In signal was detected and observed to narrow slightly with polyvinyl alcohol, but no NMR parameters could be extracted.[16] It is clear that there is a need to establish structure–spectral relationships for these important inorganic species, particularly in oxide local environments. The initial focus of this work was to demonstrate the applicability of ^{115}In and ^{209}Bi NMR to oxides, but it is noted that this report is also one of the first to describe ^{121}Sb NMR of an oxide material.[56]

For quadrupolar nuclei, it is generally desired to acquire spectra at the highest available field, B_0, to minimize the breadth of the central-transition static powder lineshape, $\Delta\nu_{CT}$, which is given from second-order perturbation theory as:

$$\Delta v_{CT} = \left(\frac{3 C_Q}{2 I (2 I - 1)} \right)^2 \cdot \left(\frac{\left(\eta_Q^2 + 22 \eta_Q + 25 \right) \left(I (I+1) - 3/4 \right)}{144 \, v_L} \right), \qquad (1)$$
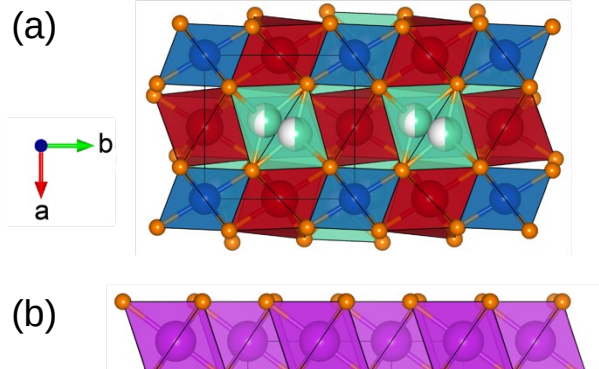
where C_Q is the quadrupolar coupling constant, η_Q is the quadrupolar asymmetry parameter, and v_L is the Larmor frequency, which is proportional to B_0.[57] Fortunately, in the case of $I = 9/2$ nuclei such as ^{115}In and ^{209}Bi, the central transition linewidths are relatively narrow (for a given C_Q) due to the I-dependence of equation (1).

The central transition (CT, $m_I = +1/2 \leftrightarrow -1/2$) of a non-integer quadrupolar nucleus is only affected by second-order quadrupolar effects while the eight satellite transitions in $I = 9/2$ nuclei (ST, $m_I = \pm 1/2 \leftrightarrow \pm 3/2, \pm 3/2 \leftrightarrow \pm 5/2, \pm 5/2 \leftrightarrow \pm 7/2, \pm 7/2 \leftrightarrow \pm 9/2$) are affected by first-, second-, and third-order quadrupolar interactions, contributing to the (ultra-)wide powder patterns expected for full (CT and ST) quadrupolar environments of ^{115}In and ^{209}Bi NMR. While second-order perturbation theory is sufficient for many quadrupolar NMR studies, numerous examples have emerged demonstrating the significance of higher-order effects.[58–65] The rule of thumb for the breakdown of second-order perturbation theory and the emergence of third-order effects is when the quadrupolar frequency v_Q given by:
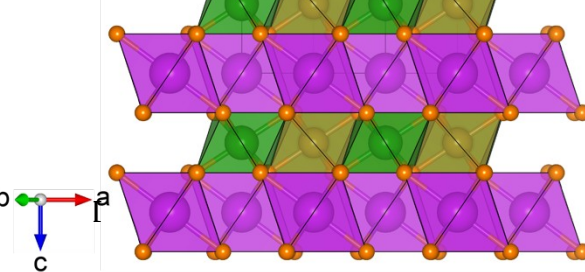
$$v_Q = \left(\frac{3 C_Q}{2 I (2 I - 1)} \right), \qquad (2)$$

approaches 10% of the Larmor frequency v_L.[66] Widdifield, Bain, and Bryce showed that even under these conditions, second-order theory would introduce underestimation errors in C_Q and δ_{iso}.[60] For large values of v_Q, the line between NMR and NQR is blurred.[67,68] The exceptionally large nuclear electric quadrupole moments of ^{113,115}In and ^{209}Bi — the largest of all main group elements — are expected to lead to noticeable third-order effects on the satellite transitions of these nuclei in distorted environments.

In this report, the ^{115}In and ^{209}Bi solid-state NMR spectra and quadrupolar parameters of three recently discovered

(a)

(b)

complex oxides (LiIn$_2$SbO$_6$, BiAlTeO$_6$, and

(ultra-)wideline NMR, periodic DFT calculations, and numerical modeling. LiIn$_2$SbO$_6$ is a

rutile-like structure with a channel arrangement

Figure 1 – Crystal structures of (a) rutile-like LiIn$_2$SbO$_6$ and (b) layered BiMTeO$_6$ (M = Al, Ga). Li$^+$ in teal, In^{3+} in red, Sb^{5+} in dark blue, Bi^{3+} in magenta, M^{3+} in green, Te^{6+} in gold, O^{2-} in orange.

1a).[19] BiAlTeO$_6$ and BiGaTeO$_6$ are isostructural

BiO$_6$ and mixed, ordered MO$_6$/TeO$_6$ (M = Al, Ga) (Figure 1b). Collection of the broad (>15

MHz) NMR spectra is facilitated by signal enhancement from the quadrupolar Carr–Purcell–

Meiboom–Gill (QCPMG) pulse sequence in combination with frequency-stepped acquisition,

also known as the variable-offset cumulative spectrum (VOCS)[69] approach. The results are

described in the context of the very different local symmetry and coordination environments

of indium and bismuth in these examples. A new synthetic route is developed to prepare a

bulk sample of crystalline BiAlTeO$_6$ suitable for NMR. Chemical shift and quadrupolar

parameters of ^{27}Al, ^{71}Ga, and ^{121}Sb NMR are also investigated and correlated to the local

geometry of these cations.

Experimental

Synthesis. LiIn$_2$SbO$_6$, BiAlTeO$_6$, and BiGaTeO$_6$ were synthesized from high-temperature

solid-state or flux methods.[19,31] Li$_2$CO$_3$ (Aldrich, 99.999%), Na$_2$CO$_3$ (Aldrich, 99.0%), In$_2$O$_3$

(Alfa Aesar, 99.994%), Sb$_2$O$_3$ (Aldrich, 99%), Bi$_2$O$_3$ (Aldrich, 99.9%), Al$_2$O$_3$ (Aldrich,

99.9%), Ga$_2$O$_3$ (Aldrich, 99.9%), and TeO$_2$ (Aldrich, 99.9%) precursors were used as

received. H$_2$TeO$_4$·2H$_2$O (Aldrich, 99.6%) was converted to amorphous TeO$_3$ through a pre-

heating step at 673 K for 12 h in air. The reagents were ground together in an agate mortar

and pestle until homogenous. LiIn$_2$SbO$_6$ was prepared by annealing the stoichiometric

pelletized reactants in a Pt crucible in air at 1173 K for 8 h followed by 1473 K for 20 h with

an intermediate regrinding. Attempts to prepare single phase BiAlTeO$_6$ via solid state

reaction with stoichiometric quantities of Al$_2$O$_3$, Bi$_2$O$_3$, and TeO$_3$ (or TeO$_2$) were

unsuccessful, as reported.[31] Thus, a Na$_2$CO$_3$–TeO$_2$ flux method demonstrated to produce

single crystals[31] of $BiAlTeO_6$ was modified to prepare a larger quantity for this work. A mixture 1:4:1 mole ratio of Na_2CO_3:TeO_2:Bi_2O_3 was placed in an alumina crucible, which provided the source of Al for $BiTeAlO_6$. The crucible was heated to 973 K, held for 5 h as a melt, cooled to 673 K at a rate of $0.1 K \cdot min^{-1}$, and then quenched to room temperature on the bench. $BiGaTeO_6$ was prepared by heating a pellet of Bi_2O_3, Ga_2O_3, and TeO_3 in a Pt crucible in air for a total of 40 h at 973 K with intermediate regrindings.

Diffraction. Powder X-ray diffraction patterns were recorded in transmission mode with a STOE Stadi P diffractometer and Cu Kα radiation. Finely ground sample powders were loaded between two sheets of Kapton tape. Diffraction patterns were recorded from 5–80˚ 2θ while the sample rotated to improve powder averaging (*nota bene*, data are displayed from 15–75˚ 2θ to more clearly show the observed reflections). Calculated patterns correspond to entries in the Inorganic Crystal Structure Database (ICSD): $LiIn_2SbO_6$ (collection code 1976010), $BiAlTeO_6$ (collection code 21784), and $BiGaTeO_6$ (collection code 21785).

Solid-state NMR. NMR spectra were recorded in a 9.4 T static magnetic field with a Bruker Avance III spectrometer and a 4.0 mm Bruker HX probe with the exception of ^{23}Na and fast MAS ^{69,71}Ga measured with a 1.6 mm Phoenix HFX probe. MAS and static ^{27}Al spectra were acquired with a Bloch decay ($\pi/2$–acq.) pulse sequence and a 1.3 µs excitation pulse corresponding to the $\pi/2$ pulse optimized on α-Al_2O_3. For ^{27}Al, a recycle delay of 6.25 s was used, corresponding to $5T_1$, and 192 scans were summed. ^{69}Ga MAS and static NMR spectra were recorded with a Hahn-echo ($\pi/2$–τ_1–π–τ_2–acq.) pulse sequence with a rotor-synchronized (MAS) or 10 µs (static) interpulse delay. ^{69,71}Ga spectra were collected with either a Bloch decay pulse sequence or a Hahn-echo pulse sequence with rotor synchronization or, for static Hahn-echo spectra, a 10 µs interpulse delay. For static and 10–

15 kHz MAS ^{69}Ga and ^{71}Ga recorded on the 4.0 mm probe, a $\dfrac{¿2}{\left(I+\dfrac{1}{2}\right)}=(¿4)_{liquid}$ excitation

pulse of 2.2 µs was applied, the recycle delays were 2 s (~$2T_1$), and 3072–12,288 scans (^{69}Ga)

or 256–560 scans (^{71}Ga) were summed. For ^{69}Ga and ^{71}Ga spectra collected at 35 kHz MAS

with the 1.6 mm probe, an excitation pulse of 1.0 µs was applied; 56,480 scans with a recycle

delay of 1 s were summed for ^{69}Ga and 17,800 scans with a recycle delay of 3 s were summed

for ^{71}Ga. ^{23}Na MAS NMR was recorded with a rotor-synchronized Hahn-echo, a 1.1 µs π/2

pulse, a 10 s recycle delay, and by summing 128 scans. Static ^{115}In, ^{121}Sb and ^{209}Bi spectra

were recorded with a frequency-stepped quadrupolar Carr–Purcell–Meiboom–Gill (QCPMG)

approach with excitation and refocusing pulses of 1.0 µs and 2.0 µs pulses, respectively, and

a spikelet spacing of 5 kHz. The excitation and refocusing pulse lengths were determined by

maximizing the ^{209}Bi central transition signal in $BiGaTeO_6$. For ^{115}In QCPMG, 21 echoes

were captured in each free induction decay, 186 spectra were collected with transmitter offset

steps of 100 kHz, the recycle delay was 0.1 s, and 256 scans were summed at each offset

frequency. For ^{209}Bi QCPMG in $BiAlTeO_6$, 21 echoes were captured in each free induction

decay, 145 spectra were collected with transmitter offset steps of 125 kHz, the recycle delay

was 0.05 s, and 16,384 scans were summed at each offset frequency. For ^{209}Bi QCPMG in

$BiGaTeO_6$, 11 echoes were captured in each free induction decay, 133 spectra were collected

with transmitter offset steps of 125 kHz, the recycle delay was 0.05 s, and 8192 scans were

summed at each offset frequency. Solid NaCl at 7.2 ppm,[70] α-Al_2O_3 (corundum) at 16.0 ppm

(C_Q = 2.38 MHz),[57,71] 1.0 M Ga(NO$_3$)$_{3(aq.)}$ at 0.0 ppm,[72] 0.1 M In(NO$_3$)$_3$ in 0.5 M HNO$_3$ at 0.0

ppm,[51,72] and saturated Bi(NO$_3$)$_3$ in concentrated HNO$_3$ at 0.0 ppm[72] were used as NMR shift

references.

Spectral Simulations. ^{27}Al, ^{69}Ga, and ^{71}Ga MAS and static solid-state NMR spectra were

simulated with second-order perturbation theory in the Solid Lineshape Analysis (SOLA)

program within TopSpin 3.6.1. Static ^{113}In, ^{115}In, ^{121}Sb, and ^{209}Bi spectra were modeled with the 'Quadrupolar Exact Software' (QUEST) numerical simulation program, which treats the combined Zeeman–quadrupole Hamiltonian exactly.[63] MagresView (v1.6.2) was used to visualize tensor orientations and calculate Euler angles.[73]

NMR Conventions. In this study, the Haeberlen convention is used to describe the chemical shift tensor with the isotropic shift $\delta_{iso} = \dfrac{\delta_{XX} + \delta_{YY} + \delta_{ZZ}}{3}$; chemical shift anisotropy $\delta_{CSA} = \delta_{ZZ} - \delta_{iso}$; and the shift asymmetry $\eta_{CSA} = \dfrac{\delta_{YY} - \delta_{XX}}{\delta_{ZZ} - \delta_{iso}}$. In this definition, the principal components of the shift tensor are ordered such that $|\delta_{ZZ} - \delta_{iso}| \geq |\delta_{XX} - \delta_{iso}| \geq |\delta_{YY} - \delta_{iso}|$. The above definition of δ_{CSA} is sometimes referred to as the reduced anisotropy, which is equal to 2/3 of the 'full' anisotropy $\Delta\delta = \delta_{ZZ} - \dfrac{\delta_{XX} + \delta_{YY}}{2}$ used by some authors and programs. The quadrupolar coupling constant C_Q is defined by the nuclear quadrupole moment Q and the largest principal component V_{ZZ} of the EFG at the nucleus according to $C_Q = \dfrac{eQV_{ZZ}}{h}$, where e is the electric charge and h is Planck's constant. The quadrupolar asymmetry parameter η_Q is defined by the EFG tensor components as $\eta_Q = \dfrac{V_{XX} - V_{YY}}{V_{ZZ}}$, with components ordered such that $|V_{ZZ}| \geq |V_{YY}| \geq |V_{XX}|$. The relative orientations of the chemical shift and quadrupolar tensors are defined by a set of Euler angles α, β, γ defined here in the (ZYZ) Rose convention.

Ab Initio Calculations. Chemical shielding and electric field gradient calculations were performed with the gauge-including projector augmented-wave (GIPAW) approach in the planewave pseudopotential code CASTEP.[74–77] The calculations used the

Perdew−Burke−Ernzerhof (PBE) exchange−correlation functional[78] and Vanderbilt ultrasoft pseudopotentials[79] with the default Koelling–Harmon scalar relativistic treatment.[80] $LiIn_2SbO_6$, $BiAlTeO_6$, and $BiGaTeO_6$ crystal structures were used as starting models.[19,31] Prior to the NMR calculations, atomic positions and lattice were optimized until the force on any atom was smaller than 1 meV $Å^{-1}$. All calculations used a planewave energy cutoff energy of 700 eV and a Monkhorst−Pack[81] grid with a spacing finer than $2\pi \times 0.03$ $Å^{-1}$ to sample the Brillouin zone. Anisotropic NMR parameters were used as the starting point to fit the experimental spectra.

Results and Discussion

Synthesis and Diffraction. Crystalline samples of $LiIn_2SbO_6$ and $BiGaTeO_6$ were synthesized by high-temperature solid-state methods while $BiAlTeO_6$ was synthesized from a flux to overcome substantial impurities observed from the previously described method.[31] Laboratory powder XRD confirmed the crystal structure and crystalline purity of each sample. A broad background component is visible in the diffraction pattern of the $BiAlTeO_6$
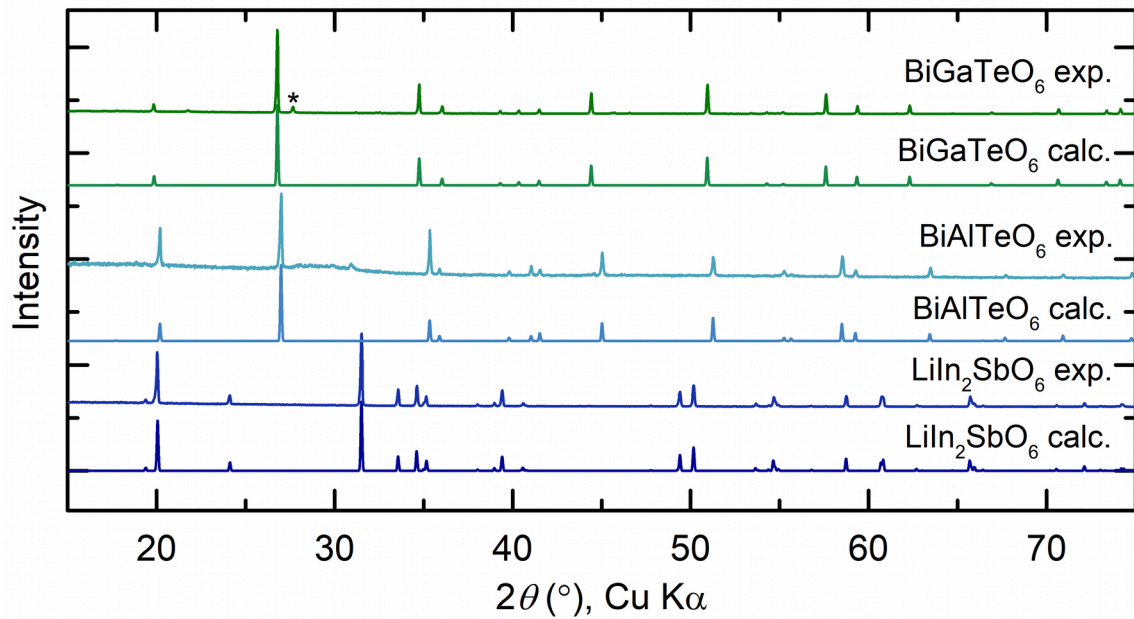

Figure 2 – Experimental and calculated X-ray diffraction patterns of $LiIn_2SbO_6$, $BiAlTeO_6$, and $BiGaTeO_6$. The asterisk in the pattern of the $BiGaTeO_6$ sample denotes an impurity peak assigned to $Bi_2Te_2O_7$.

sample. Based on the flux composition, this scattering contribution is attributed to amorphous sodium tellurates.

Solid-state NMR of LiIn₂SbO₆. A wideline solid-state [115]In NMR spectrum of LiIn₂SbO₆ was recorded by collecting frequency-stepped sub-spectra covering an excitation range of more than 18 MHz (Figure 3, Supplementary Figures S1–S3). In addition to signals from [115]In, the broadband spectrum also overlaps the [121]Sb and [113]In Larmor frequencies. While the ST intensity was visible for >15 MHz (Figure 3a), the [115]In CT linewidth was only *ca.* 400 kHz (Figure 3b, Supplementary Figure S1). At high frequencies, a quadrupolar CT lineshape from the [121]Sb site was clearly distinguished (Figure 3a, Figure 4, Supplementary Figure S2). The CT pattern of [121]Sb is an order-of-magnitude broader than the CT of [115]In due not only to the higher C_Q of the former in this sample but also the lower spin quantum number of [121]Sb ($I = 5/2$, see equation 1). The minor signal expected from [113]In at low frequency was not readily observed (Figure 3a, Supplementary Figure S3).

Planewave DFT calculations of the shielding and quadrupolar tensors provided a helpful starting point for spectral fitting. Full (CT and ST) simulations of the experimental lineshape yielded a [115]In quadrupolar coupling constant of 54.5(10) MHz with an asymmetry of 0.53(2) (Table 1). Few [115]In satellite transition discontinuities were visible, but the simulation and experiment are in reasonable agreement for the central transition and overall satellite lineshape. A [115]In isotropic shift of 130(20) ppm was determined, but the large quadrupolar interaction precluded the extraction of anisotropic chemical shift parameters at this moderate B_0 field (9.4 T). The calculated chemical shift anisotropy (Table 1) had no effect on the lineshape. The [121]Sb signal was simulated with a C_Q of 89(1) MHz and an η_Q of 0.238(5). Additional details concerning the [115]In and [121]Sb variable-offset QCPMG spectral representations are given in Supporting Figures 1 and 2, respectively.

Structure–Spectral Relationships in LiIn₂SbO₆. The single crystallographically unique indium site in $LiIn_2SbO_6$ is a distorted InO_6 octahedron with room-temperature

(a)

^{121}Sb

^{115}In

^{113}In

| 1 | 0 | −1 | v ^{121}Sb (MHz) |

| 10000 | 0 | −10000 | δ ^{121}Sb (ppm) |

Figure 4 – ^{121}Sb NMR of $LiIn_2SbO_6$. Experimental data in blue, spectral simulations in orange. The dashed orange trace is the pure ^{121}Sb contribution while the solid orange trace is from the full simulation (see Figure 3) including ^{115}In satellite transition intensity, which clearly contributes to the lineshape on the low frequency side.

| 7.5 | 5 | 2.5 | 0 | −2.5 | −5 | v ^{115}In (MHz) |

| 100000 | 50000 | 0 | −50000 | δ ^{115}In (ppm) |

(b)

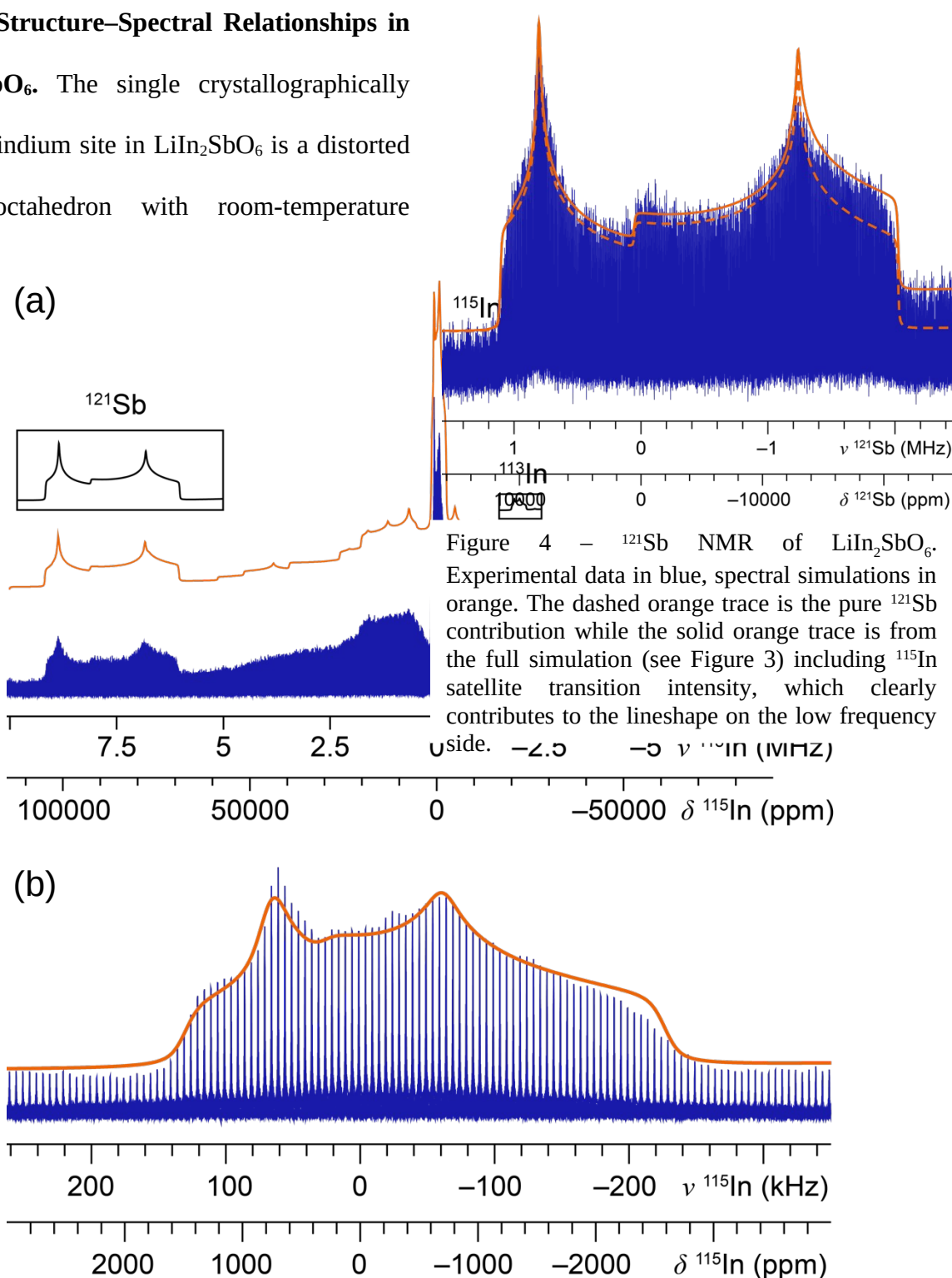| 200 | 100 | 0 | −100 | −200 | v ^{115}In (kHz) |

| 2000 | 1000 | 0 | −1000 | −2000 | δ ^{115}In (ppm) |

Figure 3 – ^{115}In NMR of $LiIn_2SbO_6$. (a) Full spectral width including the ^{115}In central and satellite transitions, ^{121}Sb central transition at high frequency and the ^{113}In central transition at low frequency (not experimentally resolved). (b) ^{115}In central transition region only. Experimental data in blue, full simulations in orange, ^{121}Sb and ^{113}In contributions to the overall lineshape inset in black. The ppm scale is relative to the ^{115}In reference compound.

bond-lengths varying from 2.10 to 2.26 Å and severely distorted bond angles.[19] Despite these

first-shell distortions, the magnitude of C_Q in LiIn$_2$SbO$_6$ [54.5(10) MHz] is substantially smaller than either indium site in bixbyite In$_2$O$_3$ [In(1) = 183(2) MHz; In(2) = 126(2) MHz].[54,55] Nevertheless, the experimental ^{115}In C_Q in the quaternary oxide is substantially larger than the DFT-predicted value. A similar phenomenon was observed for ^{121}Sb. The intermediate ^{115}In and ^{121}Sb asymmetry parameters are consistent with the lack of axial symmetry at the indium or antimony site.

One possible explanation for the deviation between the calculated and experimental results relates to disorder on the lithium site. Lithium coordination in LiIn$_2$SbO$_6$ was previously probed by ^{6}Li and ^{7}Li NMR where it was determined that the unique tunnel pattern of this rutile-like structure hosts lithium ions in split tetrahedral sites.[19] This finding ran counter to a previous proposal that LiIn$_2$SbO$_6$ is simply a cation-ordered variant of LiSbO$_3$ with octahedral LiO$_6$ sites. The ^{6,7}Li NMR, however, is unable to resolve the question of whether it is disordered (statically or dynamically) in the split tetrahedral site, which may affect the indium and antimony via next-nearest-neighbor interactions. It is also possible that the computed EFG parameters for ^{115}In and ^{121}Sb in LiIn$_2$SbO$_6$ are underestimated, which is a known issue in a variety of systems.[38,82,83]

Table 1 – Experimental and calculated ^{115}In and ^{121}Sb NMR parameters of LiIn$_2$SbO$_6$.

Nucleus	Source	σ_{iso} or δ_{iso} (ppm)^b	δ_{CSA} (ppm)	η_{CSA}	C_Q (MHz)	η_Q	α,β,γ (°)
^{115}In LiIn$_2$SbO$_6$	Calculated	σ_{iso} = 3331	−50.4	0.89	39.3	0.46	26,90,3
	Experimental^a	δ_{iso} = 130(20)	n/d	n/d	54.5(10)	0.53(2)	n/d
^{121}Sb LiIn$_2$SbO$_6$	Calculated	σ_{iso} = 2388	−96.6	0.03	58.4	0.43	0,1,0
	Experimental^a	δ_{iso} = 350(20)	n/d	n/d	89(1)	0.238(5)	n/d

^{a}Estimated uncertainty in the fit given in parentheses. ^{b}In the absence of additional ^{115}In or ^{121}Sb shift measurements, it is not yet possible to reliably convert the calculated shieldings to the experimentally observed isotropic shifts. However, the values here may prove useful in deriving future relationships.

Solid-state NMR of Bi*M*TeO$_6$ (*M* = Al, Ga). The frequency-stepped VOCS method with QCPMG pulses was also used to record (ultra-)wideline CT and partial ST spectra of BiAlTeO$_6$ and BiGaTeO$_6$ covering more than 16 MHz (Figure 5, Supplementary Figure S4). Both samples exhibit ^{209}Bi CT that are greater than 1 MHz in breadth (Supplementary Figure

(a)

S5). Numerous distinct satellite transition features were clearly resolved in the ultra-wideline spectra across the entire measured frequency range.

Once again, DFT calculations provided a valuable basis for approaching the spectral fitting. As in the case of the [115]In spectrum, the calculated shift anisotropy suggested that it would have no impact on the simulated [209]Bi linewidth at 9.4 T, and so the number of variable fitting parameters could be reduced. Note that a previous study of bismuth compounds (oxyhalides, nitrate pentahydrate, triflate, and acetate) observed chemical shift anisotropy values that were typically an order-of-magnitude [larger than the valu]es for the bismuth oxides here.[48] The quadrupolar tensor parameters were adjusted to match the discontinuities in the powder lineshape, and the quadrupolar coupling values from DFT were found to be within 5% of those determined experimentally (Table 2).
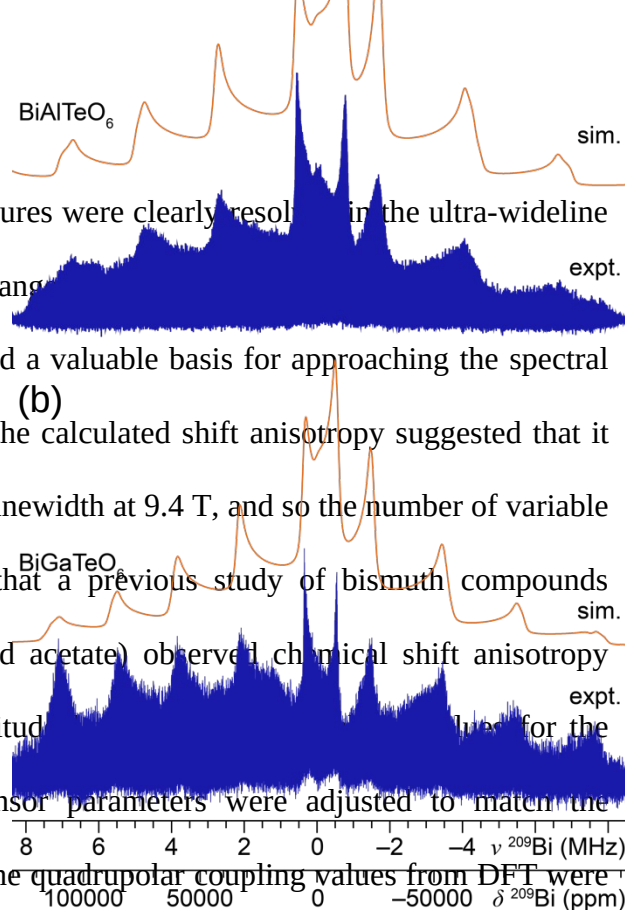

Figure 5 – [209]Bi NMR of (a) BiAlTeO$_6$ and (b) BiGaTeO$_6$. Experimental data in blue, spectral simulations in orange.

Table 2 – Experimental and calculated [209]Bi NMR parameters of BiAlTeO$_6$ and BiGaTeO$_6$.

Nucleus	Source	σ_{iso} or δ_{iso} (ppm)[b]	δ_{CSA} (ppm)	η_{CSA}	C_Q (MHz)	η_Q	α,β,γ (°)
[209]Bi BiAlTeO$_6$	Calculated	σ_{iso} = 6192	–137	0.00	106.5	0.00	1,0,116
	Experimental[a]	δ_{iso} = 1300(500)	n/d	n/d	110(2)	0.03(3)	n/d
[209]Bi BiGaTeO$_6$	Calculated	σ_{iso} = 6091	–120	0.00	93.9	0.00	19,0,142
	Experimental[a]	δ_{iso} = 1500(500)	n/d	n/d	90(2)	0.02(2)	n/d

[a]Estimated uncertainty in the fit given in parentheses. [b]In the absence of additional [209]Bi shift measurements, it is not yet possible to reliably convert the calculated shieldings to the experimentally observed isotropic shifts. However, the values here may prove useful in deriving future relationships.

NMR spectra of the quadrupolar *M*-site cations in Bi*M*TeO$_6$ were measured as further probes of the atomic structure models. ^{27}Al MAS NMR of BiAlTeO$_6$ revealed a single pseudo-Voigt lineshape with a center of gravity at 18.5 ppm (Figure 6). The calculated C_Q of 2.0 MHz yields a narrower line (by about a factor of two) than the one observed; however, the calculated C_Q is consistent with the breadth of the spinning sideband manifold (~670 kHz). Assuming this C_Q magnitude, which equates to a quadrupolar shift of *ca.* 2.2 ppm, the isotropic shift is 20.7 ppm, but the estimated error in the shift is given at 3 ppm to account for uncertainty in the relatively featureless CT lineshape (Table 3). A static ^{27}Al NMR spectrum
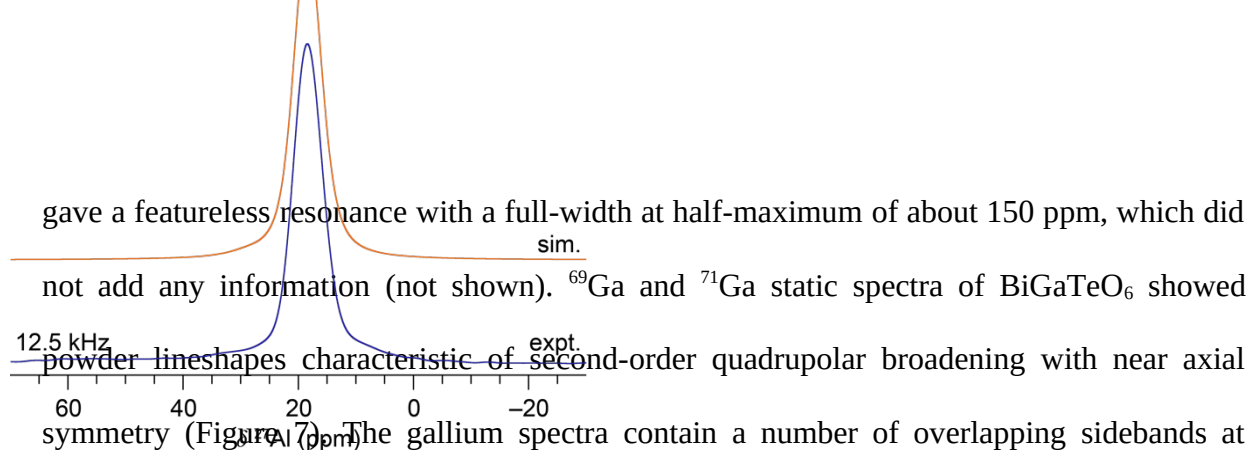
gave a featureless resonance with a full-width at half-maximum of about 150 ppm, which did

not add any information (not shown). ^{69}Ga and ^{71}Ga static spectra of BiGaTeO$_6$ showed

powder lineshapes characteristic of second-order quadrupolar broadening with near axial

symmetry (Figure 7). The gallium spectra contain a number of overlapping sidebands at

12.5 kHz

60   40   20   0   −20
δ ^{27}Al (ppm)

sim.

expt.

Figure 6 – ^{27}Al MAS NMR spectrum of
BiAlTeO$_6$. Experimental data in blue, spectral
simulation in orange.

much smaller than the CT linewidths; this problem

Ga at 35 kHz MAS (Figure 7). In each case, the

features under static and variable MAS rates could be readily simulated with second-order

perturbation theory (Table 3). The two gallium nuclei have a relative nuclear quadrupole

moment ratio of ^{69}Ga/^{71}Ga = 1.60, so collection of both datasets provides additional

constraints for the simulations.[35] The complementary datasets also enabled the estimation of

the chemical shift anisotropy, albeit data from a higher B_0 field would improve the precision.

Based on the synthesis conditions and the broad feature in the XRD of BiAlTeO$_6$, it

was hypothesized that the sample contains amorphous sodium tellurate(s). ^{23}Na MAS NMR

supports this hypothesis, showing a broad asymmetric resonance centered around −35 ppm

(Supplementary Figure S6), which is similar to reported ^{23}Na NMR of (Na$_2$O)$_x$(TeO$_2$)$_{1-x}$
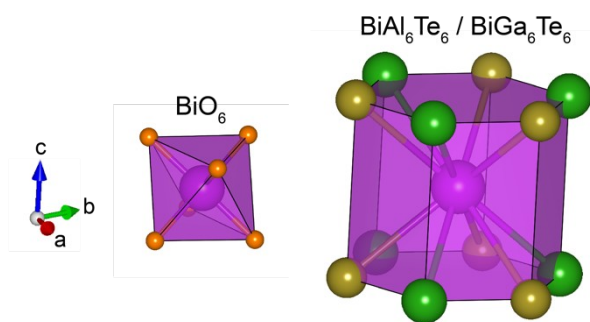
glasses.[84]

Figure 8 – First-shell coordination (BiO_6) and second-shell coordination (BiM_6Te_6, M = Al, Ga) in BiMTeO$_6$. A three-fold rotation axis runs parallel to c. Bi^{3+} in magenta, M^{3+} in green, Te^{6+} in gold, O^{2-} in orange.

Structure–Spectral Relationships in Bi*M*TeO$_6$ (*M* = Al, Ga).

BiAlTeO$_6$ and BiGaTeO$_6$ are isostructural layered compounds with a single crystallographically distinct position for each of the cations. Unlike In^{3+} in LiIn$_2$SbO$_6$, the Bi^{3+} cations in Bi*M*TeO$_6$ sit in nearly perfect octahedral symmetry with respect to the nearest-neighbor oxygen coordination. All Bi–O distances are identical, and the O–Bi–O bond angles only vary from 87.9 to 92.9°. Thus, considering only the first-shell interactions, bismuth has nearly spherical site symmetry and a small ^{209}Bi C_Q would be
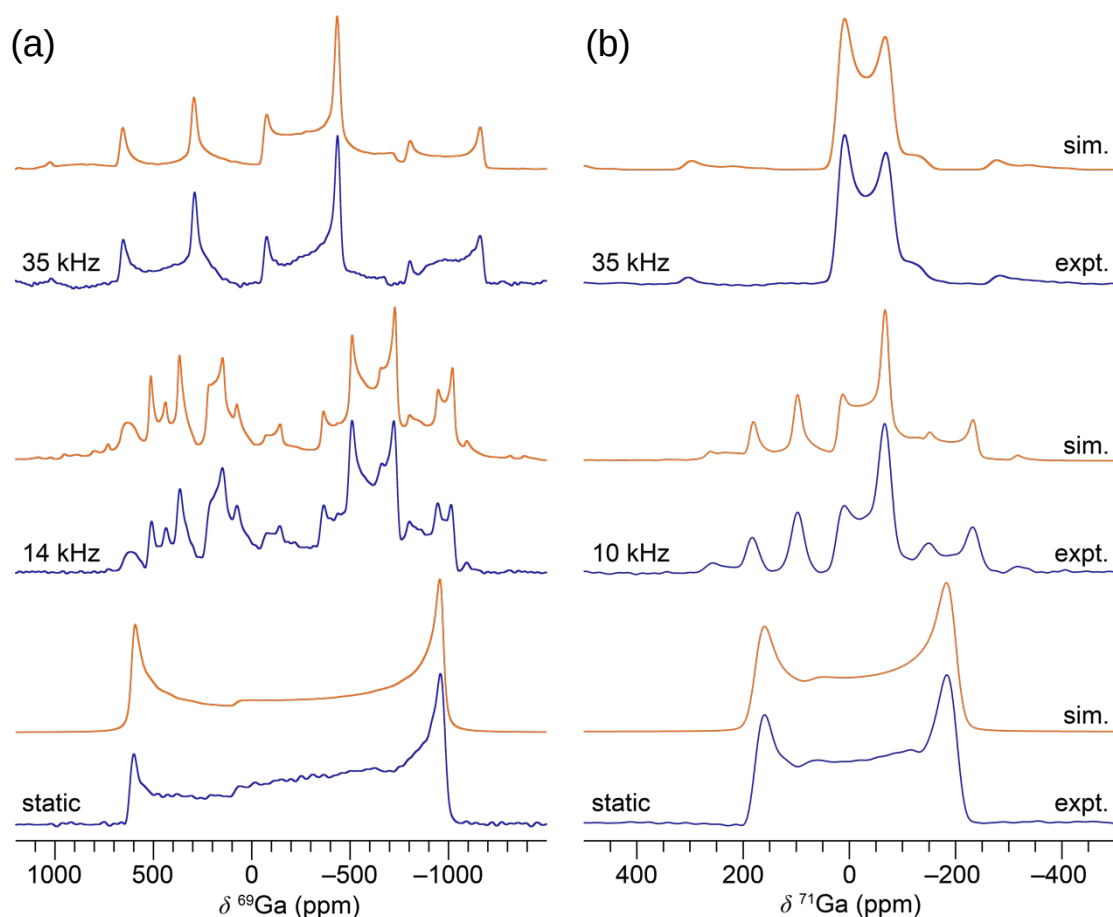

Figure 7 – (a) ^{69}Ga and (b) ^{71}Ga NMR of BiGaTeO$_6$. Experimental data in blue, spectral simulations in orange.

expected. Owing to the layered nature and chiral structure of BiMTeO$_6$, the next-nearest-neighbor (NNN, Figure 8) coordination of bismuth (*i.e.*, BiAl$_6$Te$_6$ or BiGa$_6$Te$_6$) should be considered for the origin of the observed (ultra-)wideline CT (Figure 5, Supplementary Figure S5). The NNN distances are in a narrow range from 3.844–3.846 Å but the geometry is that of a hexagonal prism. Thus, the BiAl$_6$Te$_6$ or BiGa$_6$Te$_6$ units deviate strongly from spherical symmetry; however, there is D_{3h} symmetry with the three-fold axis along the c direction (Figure 8). Accordingly, the largest component of the electric field tensor (V_{33}) at the bismuth nucleus is oriented along c. The same symmetry properties and V_{33} orientation are true for gallium and, in principle, aluminum. The dominant role of NNN effects in BiMTeO$_6$ are proposed as the explanation for the relatively small ^{209}Bi C_Qs [BiAlTeO$_6$ = 110(2) MHz; BiGaTeO$_6$ = 90(2) MHz] as compared to α-Bi$_2$O$_3$ [Bi(1) = 342.7 MHz; Bi(2) = 311.9 MHz][85] with strongly distorted BiO$_6$ octahedra. Excellent agreement between the calculated and experimentally observed quadrupolar parameters for the bismuth site in BiMTeO$_6$ strengthen the structural model and suggest the absence of significant aperiodic phenomena such as cation disorder. The calculated gallium quadrupolar parameters are underestimated, but this was systematically observed by Middlemiss *et al.* for a large number of gallates, suggesting an underlying problem that is not unique to BiGaTeO$_6$.[86]

Table 3 – Experimental and calculated ^{27}Al and ^{69,71}Ga NMR parameters of BiAlTeO$_6$ and BiGaTeO$_6$.

Nucleus	Source	δ_{iso} (ppm)	δ_{CSA} (ppm)	η_{CSA}	C_Q (MHz)	η_Q	α,β,γ (°)
^{27}Al BiAlTeO$_6$	Calculated	29[b]	10.0	0.00	2.02	0.00	78,9,35
	Experimental[a]	21(3)	n/d	n/d	≤2.0	n/d	n/d
^{69,71}Ga BiGaTeO$_6$	Calculated	85[c]	20.3	0.00	^{69}Ga = 8.14;[d] ^{71}Ga = 5.09	0.00	–71, 0, 147
	Experimental[a]	45(3)	40(20)	n/d	^{69}Ga =10.7(1);[d] ^{71}Ga = 6.68(10)	0.00(3)	n/d

[a]Estimated uncertainty in the fit given in parentheses. [b]Calculated ^{27}Al shielding converted to shift according to the expression $\delta_{iso} = m\sigma_{iso} + \sigma_{ref.}$ where m = –1.027 and $\sigma_{ref.}$ = 572.35 ppm from Seymour *et al.*[87] [c]Calculated ^{69,71}Ga shielding converted to shift according to the previous expression where m = –0.867 and $\sigma_{ref.}$ = 1502.63 ppm from Middlemiss *et al.*[86] [d]The ^{69}Ga quadrupolar coupling constant is

fixed relative to the ^{71}Ga C_Q according to the ratio of the ^{69}Ga/^{71}Ga nuclear electric quadrupole moments, which is 17.1/10.7 = 1.60.[35]

Higher-order Quadrupolar Effects. Third-order quadrupolar interactions are known to affect satellite transition frequencies in strongly quadrupolar systems. Despite ^{115}In having the largest nuclear electric quadrupole moment of the nuclei studied in this work and ^{209}Bi sites possessing the largest C_Qs, it was ^{121}Sb that deviated the most from the high-field approximation. Owing to the relatively small spin quantum number, the ^{121}Sb ($I = 5/2$) nucleus in LiIn$_2$SbO$_6$ has a ν_Q/ν_L ratio of 0.14. QUEST software was used to simulate these static spectra with an exact treatment of the Zeeman–quadrupole interaction,[63] but these results suggest that the effects would have been negligible in the spin-9/2 spectra.

Conclusions

^{115}In and ^{209}Bi solid-state NMR spectra and quadrupolar tensor quantities were reported for a series of quaternary oxides. These rarely studied $I = 9/2$ nuclei are common in a wide range of technologically important oxide materials, and this work demonstrates that quantitative information regarding first- and second-shell coordination environments can be obtained with standard solid-state NMR tools and approaches. The central transition ^{115}In spectrum of the distorted In^{3+} site in LiIn$_2$SbO$_6$ was collected in less than 5 minutes and the ultra-wideline central transition of ^{209}Bi in BiMTeO$_6$ (M= Al, Ga) required only 2–3 hours, all at a modest B_0 field of 9.4 T. Satellite transition intensity was measured out to 15–20 MHz with QCPMG for signal enhancement and the VOCS method to overcome excitation bandwidth limitations. Collecting satellite transition data is not routinely necessary but provides more precise quadrupolar coupling parameters and can reveal interesting third-order quadrupolar interaction effects in strongly coupled systems. Though not required, as demonstrated here, automated tuning software/hardware can facilitate the collection of ultra-wideline spectra. Application of adiabatic wideline, uniform rate, smooth truncation

(WURST) pulses could further decrease the instrument time in future studies.[88–90] Finally, DFT calculations are particularly powerful as a predictive tool when studying systems with large quadrupolar coupling interactions. Simulations of the expected lineshape facilitate the design of suitable experiments, *e.g.*, echo vs. QCPMG, QCPMG spikelet spacing, VOCS spacing, spectrometer time required, and the consequences of different field strengths.

Author Information

Corresponding Author

Email: kentjgriffith@gmail.com

Notes

The authors declare no competing financial interest.

Data underlying this manuscript are available for download at https://doi.org/10.6084/m9.figshare.14478168.

Acknowledgements

References

(1)   Bel Hadj Tahar, R.; Ban, T.; Ohya, Y.; Takahashi, Y. Tin Doped Indium Oxide Thin Films: Electrical Properties. *J. Appl. Phys.* **1998**, *83* (5), 2631–2645. https://doi.org/10.1063/1.367025.

(2)   Bizo, L.; Choisnet, J.; Retoux, R.; Raveau, B. The Great Potential of Coupled Substitutions in In_2O_3 for the Generation of Bixbyite-Type Transparent Conducting Oxides, $In_{2-2x}M_xSn_xO_3$. *Solid State Commun.* **2005**, *136* (3), 163–168. https://doi.org/10.1016/j.ssc.2005.07.009.

(3)   Hoel, C. A.; Mason, T. O.; Gaillard, J.-F.; Poeppelmeier, K. R. Transparent Conducting Oxides in the $ZnO–In_2O_3–SnO_2$ System. *Chem. Mater.* **2010**, *22* (12), 3569–3579. https://doi.org/10.1021/cm1004592.

(4)   Granqvist, C. G.; Hultåker, A. Transparent and Conducting ITO Films: New Developments and Applications. *Thin Solid Films* **2002**, *411* (1), 1–5. https://doi.org/10.1016/S0040-6090(02)00163-3.

(5)   Betz, U.; Kharrazi Olsson, M.; Marthy, J.; Escolá, M. F.; Atamny, F. Thin Films Engineering of Indium Tin Oxide: Large Area Flat Panel Displays Application. *Surf. Coat. Technol.* **2006**, *200* (20–21), 5751–5759. https://doi.org/10.1016/j.surfcoat.2005.08.144.

(6)   Garcia, G.; Buonsanti, R.; Llordes, A.; Runnerstrom, E. L.; Bergerud, A.; Milliron, D. J. Near-Infrared Spectrally Selective Plasmonic Electrochromic Thin Films. *Adv. Opt. Mater.* **2013**, *1* (3), 215–220. https://doi.org/10.1002/adom.201200051.

(7)   Granqvist, C. G. Electrochromics for Smart Windows: Oxide-Based Thin Films and Devices. *Thin Solid Films* **2014**, *564* (Supplement C), 1–38. https://doi.org/10.1016/j.tsf.2014.02.002.

(8)   Maho, A.; Saez Cabezas, C. A.; Meyertons, K. A.; Reimnitz, L. C.; Sahu, S.; Helms, B. A.; Milliron, D. J. Aqueous Processing and Spray Deposition of Polymer-Wrapped Tin-Doped Indium Oxide Nanocrystals as Electrochromic Thin Films. *Chem. Mater.* **2020**, *32* (19), 8401–8411. https://doi.org/10.1021/acs.chemmater.0c02399.

(9)   Cheng, P.; Zhan, X. Stability of Organic Solar Cells: Challenges and Strategies. *Chem. Soc. Rev.* **2016**, *45* (9), 2544–2582. https://doi.org/10.1039/C5CS00593K.

(10)   Chen, S.; Wang, Y.; Zhang, L.; Zhao, J.; Chen, Y.; Zhu, D.; Yao, H.; Zhang, G.; Ma, W.; Friend, R. H.; Chow, P. C. Y.; Gao, F.; Yan, H. Efficient Nonfullerene Organic Solar Cells with Small Driving Forces for Both Hole and Electron Transfer. *Adv. Mater.* **2018**, *30* (45), 1804215. https://doi.org/10.1002/adma.201804215.

(11)   Way, A.; Luke, J.; Evans, A. D.; Li, Z.; Kim, J.-S.; Durrant, J. R.; Hin Lee, H. K.; Tsoi, W. C. Fluorine Doped Tin Oxide as an Alternative of Indium Tin Oxide for Bottom Electrode of Semi-Transparent Organic Photovoltaic Devices. *AIP Adv.* **2019**, *9* (8), 085220. https://doi.org/10.1063/1.5104333.

(12)   Godinho, K. G.; Morgan, B. J.; Allen, J. P.; Scanlon, D. O.; Watson, G. W. Chemical Bonding in Copper-Based Transparent Conducting Oxides: $CuMO_2$ (*M* = In, Ga, Sc). *J. Phys. Condens. Matter* **2011**, *23* (33), 334201. https://doi.org/10.1088/0953-8984/23/33/334201.

(13)   Kim, M.-G.; Kanatzidis, M. G.; Facchetti, A.; Marks, T. J. Low-Temperature Fabrication of High-Performance Metal Oxide Thin-Film Electronics via Combustion Processing. *Nat. Mater.* **2011**, *10* (5), 382–388. https://doi.org/10.1038/nmat3011.

(14)   Rickert, K.; Huq, A.; Lapidus, S. H.; Wustrow, A.; Ellis, D. E.; Poeppelmeier, K. R. Site Dependency of the High Conductivity of $Ga_2In_6Sn_2O_{16}$: The Role of the 7-Coordinate Site. *Chem. Mater.* **2015**, *27* (23), 8084–8093. https://doi.org/10.1021/acs.chemmater.5b03790.

(15)   Flynn, S.; Adekoya, A. J.; Saeed, S.; Zhang, C.; Dravid, V. P.; Gonzalez, G. B.; Poeppelmeier, K. R. $(Cu_xZn_{1-x})_{0.456}In_{1.084}Ge_{0.46}O_3$ $(0 \leq x \leq 1)$: A Complex, Ordered, Anion-Deficient Fluorite with Unusual Site-Specific Cation Mixing. *Inorg. Chem.* **2019**, *58* (22), 15610–15617. https://doi.org/10.1021/acs.inorgchem.9b02692.

(16)   Huang, W.; Chien, P.-H.; McMillen, K.; Patel, S.; Tedesco, J.; Zeng, L.; Mukherjee, S.; Wang, B.; Chen, Y.; Wang, G.; Wang, Y.; Gao, Y.; Bedzyk, M. J.; DeLongchamp, D. M.; Hu, Y.-Y.; Medvedeva, J. E.; Marks, T. J.; Facchetti, A. Experimental and Theoretical Evidence for Hydrogen Doping in Polymer Solution-Processed Indium Gallium Oxide. *Proc. Natl. Acad. Sci.* **2020**, 202007897. https://doi.org/10.1073/pnas.2007897117.

(17)   Naganovsky, Y. K.; Sigaryov, S. E. "Rigid" Skeleton Dynamics of $Li_3In_2(PO_4)_3$ Superionic Conductor. *Solid State Ion.* **1992**, *50* (1–2), 1–9. https://doi.org/10.1016/0167-2738(92)90030-S.

(18)   Zhao, X.; Zhang, Z.; Zhang, X.; Tang, B.; Xie, Z.; Zhou, Z. Computational Screening and First-Principles Investigations of NASICON-Type $Li_xM_2(PO_4)_3$ as Solid Electrolytes for Li Batteries. *J. Mater. Chem. A* **2018**, *6* (6), 2625–2631. https://doi.org/10.1039/C7TA08968F.

(19)   Flynn, S.; Sanghvi, S.; Nisbet, M. L.; Griffith, K. J.; Zhang, W.; Halasyamani, P. S.; Haile, S. M.; Poeppelmeier, K. R. $LiIn_2SbO_6$: A New Rutile-Related Structure Type with Unique Ion Channels. *Chem. Mater.* **2020**, *32* (11), 4785–4794. https://doi.org/10.1021/acs.chemmater.0c01491.

(20)   P. Shuk; Hans-Dieter Wiemhöfer; U. Guth; W. Göpel; Martha Greenblatt. Oxide Ion Conducting Solid Electrolytes Based on Bi_2O_3. *Solid State Ion.* **1996**, *89* (3–4), 179–196. https://doi.org/10.1016/0167-2738(96)00348-7.

(21)   Takahashi, T.; Iwahara, H.; Nagai, Y. High Oxide Ion Conduction in Sintered Bi_2O_3 Containing SrO, CaO or La_2O_3. *J. Appl. Electrochem.* **1972**, *2*, 97–104.

(22)   Kuang, X.; Payne, J. L.; Johnson, M. R.; Radosavljevic Evans, I. Remarkably High Oxide Ion Conductivity at Low Temperature in an Ordered Fluorite-Type Superstructure. *Angew. Chem. Int. Ed.* **2012**, *51* (3), 690–694. https://doi.org/10.1002/anie.201106111.

(23)   Dunstan, M. T.; Halat, D. M.; Tate, M. L.; Evans, I. R.; Grey, C. P. Variable-Temperature Multinuclear Solid-State NMR Study of Oxide Ion Dynamics in Fluorite-Type Bismuth Vanadate and Phosphate Solid Electrolytes. *Chem. Mater.* **2019**, *31* (5), 1704–1714. https://doi.org/10.1021/acs.chemmater.8b05143.

(24)   Goodenough, J. B.; Manthiram, A.; Paranthaman, P.; Zhen, Y. S. Fast Oxide-Ion Conduction in Intergrowth Structures. *Solid State Ion.* **1992**, *52* (1–3), 105–109. https://doi.org/10.1016/0167-2738(92)90096-8.

(25)   Kim, N.; Grey, C. P. Probing Oxygen Motion in Disordered Anionic Conductors with ^{17}O and [51]V MAS NMR Spectroscopy. *Science* **2002**, *297* (5585). https://doi.org/10.1126/science.1074130.

(26)   Guignard, M.; Albrecht, L.; Zwanziger, J. W. Zero-Stress Optic Glass without Lead. *Chem. Mater.* **2007**, *19* (2), 286–290. https://doi.org/10.1021/cm062208a.

(27)   Maeder, T. Review of Bi_2O_3 Based Glasses for Electronics and Related Applications. *Int. Mater. Rev.* **2013**, *58* (1), 3–40. https://doi.org/10.1179/1743280412Y.0000000010.

(28)   Vehkamäki, M.; Hatanpää, T.; Kemell, M.; Ritala, M.; Leskelä, M. Atomic Layer Deposition of Ferroelectric Bismuth Titanate $Bi_4Ti_3O_{12}$. *Chem. Mater.* **2006**, *18* (16), 3883–3888. https://doi.org/10.1021/cm060966v.

(29)   Singh, D. J.; Seo, S. S. A.; Lee, H. N. Optical Properties of Ferroelectric $Bi_4Ti_3O_{12}$. *Phys. Rev. B* **2010**, *82* (18), 180103(R). https://doi.org/10.1103/PhysRevB.82.180103.

(30) Kim, H. G.; Tran, T. T.; Choi, W.; You, T.-S.; Halasyamani, P. S.; Ok, K. M. Two New Non-Centrosymmetric n = 3 Layered Dion−Jacobson Perovskites: Polar $RbBi_2Ti_2NbO_{10}$ and Nonpolar $CsBi_2Ti_2TaO_{10}$. *Chem. Mater.* **2016**, *28* (7), 2424–2432. https://doi.org/10.1021/acs.chemmater.6b00778.

(31) Ding, F.; Nisbet, M. L.; Yu, H.; Zhang, W.; Chai, L.; Halasyamani, P. S.; Poeppelmeier, K. R. Syntheses, Structures, and Properties of Non-Centrosymmetric Quaternary Tellurates $BiMTeO_6$ (M = Al, Ga). *Inorg. Chem.* **2018**, *57* (13), 7950–7956. https://doi.org/10.1021/acs.inorgchem.8b01087.

(32) Ok, K. M. Functional Layered Materials with Heavy Metal Lone Pair Cations, Pb^{2+}, Bi^{3+}, and Te^{4+}. *Chem. Commun.* **2019**, *55* (85), 12737–12748. https://doi.org/10.1039/C9CC06778G.

(33) Schurko, R. W. Ultra-Wideline Solid-State NMR Spectroscopy. *Acc. Chem. Res.* **2013**, *46* (9), 1985–1995. https://doi.org/10.1021/ar400045t.

(34) Apperley, D. C.; Harris, R. K.; Hodgkinson, P. *Solid-State NMR: Basic Principles and Practice*; Monumentum Press: New York, NY, 2012.

(35) Pyykkö, P. Year-2017 Nuclear Quadrupole Moments. *Mol. Phys.* **2018**, *116* (10), 1328–1338. https://doi.org/10.1080/00268976.2018.1426131.

(36) Lo, A. Y. H.; Bitterwolf, T. E.; Macdonald, C. L. B.; Schurko, R. W. Solid-State ^{93}Nb and ^{13}C NMR Investigations of Half-Sandwich Niobium(I) and Niobium(V) Cyclopentadienyl Complexes. *J. Phys. Chem. A* **2005**, *109* (32), 7073–7087. https://doi.org/10.1021/jp0521499.

(37) Lapina, O. B.; Khabibulin, D. F.; Shubin, A. A.; Terskikh, V. V. Practical Aspects of ^{51}V and ^{93}Nb Solid-State NMR Spectroscopy and Applications to Oxide Materials. *Prog. Nucl. Magn. Reson. Spectrosc.* **2008**, *53* (3), 128–191. https://doi.org/10.1016/j.pnmrs.2007.12.001.

(38) Hanna, J. V.; Pike, K. J.; Charpentier, T.; Kemp, T. F.; Smith, M. E.; Lucier, B. E. G.; Schurko, R. W.; Cahill, L. S. A ^{93}Nb Solid-State NMR and Density Functional Theory Study of Four- and Six-Coordinate Niobate Systems. *Chem. – Eur. J.* **2010**, *16* (10), 3222–3239. https://doi.org/10.1002/chem.200901581.

(39) Johnston, K. E.; Griffin, J. M.; Walton, R. I.; Dawson, D. M.; Lightfoot, P.; Ashbrook, S. E. ^{93}Nb NMR and DFT Investigation of the Polymorphs of $NaNbO_3$. *Phys. Chem. Chem. Phys.* **2011**, *13* (16), 7565–7576. https://doi.org/10.1039/C1CP20258H.

(40) Papulovskiy, E.; Shubin, A. A.; Terskikh, V. V.; Pickard, C. J.; Lapina, O. B. Theoretical and Experimental Insights into Applicability of Solid-State ^{93}Nb NMR in Catalysis. *Phys. Chem. Chem. Phys.* **2013**, *15* (14), 5115–5131. https://doi.org/10.1039/C3CP44016H.

(41) Griffith, K. J.; Hope, M. A.; Reeves, P. J.; Anayee, M.; Gogotsi, Y.; Grey, C. P. Bulk and Surface Chemistry of the Niobium MAX and MXene Phases from Multinuclear Solid-State NMR Spectroscopy. *J. Am. Chem. Soc.* **2020**. https://doi.org/10.1021/jacs.0c09044.

(42) Tomita, Y.; Yamada, K.; Ohki, H.; Okuda, T. Structure and Dynamics of Li_3InBr_6 and $NaInBr_4$ by Means of Nuclear Magnetic Resonance. *Z. Für Naturforschung A* **1998**, *53* (6–7). https://doi.org/10.1515/zna-1998-6-730.

(43) Tomita, Y.; Yonekura, H.; Yamauchi, Y.; Yamada, K.; Kobayashi, K. Substitution Effect in the Ion Conductor Li_3InBr_6, Studied by Nuclear Magnetic Resonance. *Z. Für Naturforschung A* **2002**, *57* (6–7), 447–450. https://doi.org/10.1515/zna-2002-6-728.

(44) Yamada, K.; Kumano, K.; Okuda, T. Conduction Path of the Sodium Ion in Na_3InCl_6 Studied by X-Ray Diffraction and ^{23}Na and ^{115}In NMR. *Solid State Ion.* **2005**, *176* (7–8), 823–829. https://doi.org/10.1016/j.ssi.2004.10.016.

(45) Yamada, K.; Kumano, K.; Okuda, T. Lithium Superionic Conductors Li_3InBr_6 and $LiInBr_4$ Studied by ^7Li, ^{115}In NMR. *Solid State Ion.* **2006**, *177* (19–25), 1691–1695. https://doi.org/10.1016/j.ssi.2006.06.026.

(46) Scholz, G.; Krahl, T.; Ahrens, M.; Martineau, C.; Buzaré, J. Y.; Jäger, C.; Kemnitz, E. ^{115}In and ^{19}F MAS NMR Study of $(NH_4)_3InF_6$ Phases. *J. Fluor. Chem.* **2011**, *132* (4), 244–249. https://doi.org/10.1016/j.jfluchem.2011.01.010.

(47) Karmakar, A.; Bernard, G. M.; Meldrum, A.; Oliynyk, A. O.; Michaelis, V. K. Tailorable Indirect to Direct Band-Gap Double Perovskites with Bright White-Light Emission: Decoding Chemical Structure Using Solid-State NMR. *J. Am. Chem. Soc.* **2020**, *142* (24), 10780–10793. https://doi.org/10.1021/jacs.0c02198.

(48) Hamaed, H.; Laschuk, M. W.; Terskikh, V. V.; Schurko, R. W. Application of Solid-State ^{209}Bi NMR to the Structural Characterization of Bismuth-Containing Materials. *J. Am. Chem. Soc.* **2009**, *131* (23), 8271–8279. https://doi.org/10.1021/ja901347k.

(49) Hamaed, H.; Johnston, K. E.; Cooper, B. F. T.; Terskikh, V. V.; Ye, E.; Macdonald, C. L. B.; Arnold, D. C.; Schurko, R. W. A ^{115}In Solid-State NMR Study of Low Oxidation-State Indium Complexes. *Chem Sci* **2014**, *5* (3), 982–995. https://doi.org/10.1039/C3SC52809J.

(50) Chen, F.; Ma, G.; Bernard, G. M.; Cavell, R. G.; McDonald, R.; Ferguson, M. J.; Wasylishen, R. E. Solid-State ^{115}In and ^{31}P NMR Studies of Triarylphosphine Indium Trihalide Adducts. *J. Am. Chem. Soc.* **2010**, *132* (15), 5479–5493. https://doi.org/10.1021/ja100625p.

(51) Chen, F.; Ma, G.; Cavell, R. G.; Terskikh, V. V.; Wasylishen, R. E. Solid-State ^{115}In NMR Study of Indium Coordination Complexes. *Chem. Commun.* **2008**, No. 45, 5933. https://doi.org/10.1039/b814326a.

(52) Lo, A. Y. H.; Jurca, T.; Richeson, D. S.; Bryce, D. L. Multinuclear Solid-State Magnetic Resonance Study of In^+ and Ag^+ in Neutral Weakly Coordinating Environments. *J. Phys. Chem. Lett.* **2010**, *1* (20), 3078–3084. https://doi.org/10.1021/jz101241r.

(53) Wasylishen, R. E.; Wright, K. C.; Eichele, K.; Cameron, T. S. Characterization of the $J(^{115}In,^{31}P)$ Tensor for a 1:1 Adduct of Indium Tribromide and a Triarylphosphine. *Inorg. Chem.* **1994**, *33* (3), 407–408. https://doi.org/10.1021/ic00081a003.

(54) Yamada, K.; Yamaguchi, T.; Ohashi, R.; Ohki, S.; Deguchi, K.; Hashi, K.; Goto, A.; Shimizu, T. Field-Stepwise-Swept QCPMG Solid-State ^{115}In NMR of Indium Oxide. *Solid State Nucl. Magn. Reson.* **2020**, *109*, 101688. https://doi.org/10.1016/j.ssnmr.2020.101688.

(55) Bastow, T. J.; Whitfield, H. J. Nuclear Quadrupole Resonance of ^{69}Ga and ^{115}In in Chalcogenides MX and M_2X_3. *J. Magn. Reson.* **1975**, *20* (1), 1–10. https://doi.org/10.1016/0022-2364(75)90144-4.

(56) Faucher, A.; Terskikh, V. V.; Wasylishen, R. E. Feasibility of Arsenic and Antimony NMR Spectroscopy in Solids: An Investigation of Some Group 15 Compounds. *Solid State Nucl. Magn. Reson.* **2014**, *61–62*, 54–61. https://doi.org/10.1016/j.ssnmr.2014.05.005.

(57) Mackenzie, K. J. D.; Smith, M. E. *Multinuclear Solid-State NMR of Inorganic Materials*; Pergamon Materials Series; Pergamon: London, 2002; Vol. 6.

(58) Gan, Z.; Srinivasan, P.; Quine, J. R.; Steuernagel, S.; Knott, B. Third-Order Effect in Solid-State NMR of Quadrupolar Nuclei. *Chem. Phys. Lett.* **2003**, *367* (1–2), 163–169. https://doi.org/10.1016/S0009-2614(02)01681-0.

(59) Widdifield, C. M.; Bryce, D. L. Solid-State ^{127}I NMR and GIPAW DFT Study of Metal Iodides and Their Hydrates: Structure, Symmetry, and Higher-Order Quadrupole-

Induced Effects. *J. Phys. Chem. A* **2010**, *114* (40), 10810–10823. https://doi.org/10.1021/jp108237x.

(60) Widdifield, C. M.; Bain, A. D.; Bryce, D. L. Definitive Solid-State [185/187]Re NMR Spectral Evidence for and Analysis of the Origin of High-Order Quadrupole-Induced Effects for I = 5/2. *Phys. Chem. Chem. Phys.* **2011**, *13* (27), 12413. https://doi.org/10.1039/c1cp20572b.

(61) Attrell, R. J.; Widdifield, C. M.; Korobkov, I.; Bryce, D. L. Weak Halogen Bonding in Solid Haloanilinium Halides Probed Directly via Chlorine-35, Bromine-81, and Iodine-127 NMR Spectroscopy. *Cryst. Growth Des.* **2012**, *12* (3), 1641–1653. https://doi.org/10.1021/cg201683p.

(62) Perras, F. A.; Bryce, D. L. Direct Investigation of Covalently Bound Chlorine in Organic Compounds by Solid-State [35]Cl NMR Spectroscopy and Exact Spectral Line-Shape Simulations. *Angew. Chem. Int. Ed.* **2012**, *51* (17), 4227–4230. https://doi.org/10.1002/anie.201200728.

(63) Perras, F. A.; Widdifield, C. M.; Bryce, D. L. QUEST—QUadrupolar Exact SofTware: A Fast Graphical Program for the Exact Simulation of NMR and NQR Spectra for Quadrupolar Nuclei. *Solid State Nucl. Magn. Reson.* **2012**, *45–46*, 36–44. https://doi.org/10.1016/j.ssnmr.2012.05.002.

(64) Widdifield, C. M.; Perras, F. A.; Bryce, D. L. Solid-State [185/187]Re NMR and GIPAW DFT Study of Perrhenates and $Re_2(CO)_{10}$: Chemical Shift Anisotropy, NMR Crystallography, and a Metal–Metal Bond. *Phys. Chem. Chem. Phys.* **2015**, *17* (15), 10118–10134. https://doi.org/10.1039/C5CP00602C.

(65) Pecher, O.; Halat, D. M.; Lee, J.; Liu, Z.; Griffith, K. J.; Braun, M.; Grey, C. P. Enhanced Efficiency of Solid-State NMR Investigations of Energy Materials Using an External Automatic Tuning/Matching (EATM) Robot. *J. Magn. Reson.* **2017**, *275*, 127–136. https://doi.org/10.1016/j.jmr.2016.12.008.

(66) Bryce, D. L.; Wasylishen, R. E. Quadrupolar Nuclei in Solids: Influence of Different Interactions on Spectra. In *Encyclopedia of Magnetic Resonance*; Harris, R. K., Ed.; John Wiley & Sons, Ltd: Chichester, UK, 2011. https://doi.org/10.1002/9780470034590.emrstm1197.

(67) Bain, A. D.; Khasawneh, M. From NQR to NMR: The Complete Range of Quadrupole Interactions. *Concepts Magn. Reson.* **2004**, *22A* (2), 69–78. https://doi.org/10.1002/cmr.a.20013.

(68) Bain, A. D. Quadrupole Interactions: NMR, NQR, and in between from a Single Viewpoint. *Magn. Reson. Chem.* **2017**, *55* (3), 198–205. https://doi.org/10.1002/mrc.4418.

(69) Massiot, D.; Farnan, I.; Gautier, N.; Trumeau, D.; Trokiner, A.; Coutures, J. P. [71]Ga and [69]Ga Nuclear Magnetic Resonance Study of β-Ga_2O_3: Resolution of Four- and Six-Fold Coordinated Ga Sites in Static Conditions. *Solid State Nucl. Magn. Reson.* **1995**, *4*, 241–248. https://doi.org/10.1016/0926-2040(95)00002-8.

(70) Allan, P. K.; Griffin, J. M.; Darwiche, A.; Borkiewicz, O. J.; Wiaderek, K. M.; Chapman, K. W.; Morris, A. J.; Chupas, P. J.; Monconduit, L.; Grey, C. P. Tracking Sodium-Antimonide Phase Transformations in Sodium-Ion Anodes: Insights from Operando Pair Distribution Function Analysis and Solid-State NMR Spectroscopy. *J. Am. Chem. Soc.* **2016**, *138* (7), 2352–2365. https://doi.org/10.1021/jacs.5b13273.

(71) Jakobsen, H. J.; Skibsted, J.; Bildsøe, H.; Nielsen, N. Chr. Magic-Angle Spinning NMR Spectra of Satellite Transitions for Quadrupolar Nuclei in Solids. *J. Magn. Reson.* **1989**, *85*, 173–180.

(72) Harris, R. K.; Becker, E. D.; Cabral de Menezes, S. M.; Granger, P.; Hoffman, R. E.; Zilm, K. W. Further Conventions for NMR Shielding and Chemical Shifts (IUPAC

Recommendations 2008). *Pure Appl. Chem.* **2008**, *80* (1), 59–84. https://doi.org/10.1351/pac200880010059.

(73) Sturniolo, S.; Green, T. F. G.; Hanson, R. M.; Zilka, M.; Refson, K.; Hodgkinson, P.; Brown, S. P.; Yates, J. R. Visualization and Processing of Computed Solid-State NMR Parameters: MagresView and MagresPython. *Solid State Nucl. Magn. Reson.* **2016**, *78*, 64–70. https://doi.org/10.1016/j.ssnmr.2016.05.004.

(74) Clark, S. J.; Segall, M. D.; Pickard, C. J.; Hasnip, P. J.; Probert, M. I. J.; Refson, K.; Payne, M. C. First Principles Methods Using CASTEP. *Z. Für Krist.* **2005**, *220* (5–6), 567–570. https://doi.org/10.1524/zkri.220.5.567.65075.

(75) Pickard, C. J.; Mauri, F. All-Electron Magnetic Response with Pseudopotentials: NMR Chemical Shifts. *Phys. Rev. B* **2001**, *63* (24), 245101. https://doi.org/10.1103/PhysRevB.63.245101.

(76) Yates, J. R.; Pickard, C. J.; Mauri, F. Calculation of NMR Chemical Shifts for Extended Systems Using Ultrasoft Pseudopotentials. *Phys. Rev. B* **2007**, *76* (2), 024401. https://doi.org/10.1103/PhysRevB.76.024401.

(77) Profeta, M.; Mauri, F.; Pickard, C. J. Accurate First Principles Prediction of ^{17}O NMR Parameters in SiO_2: Assignment of the Zeolite Ferrierite Spectrum. *J. Am. Chem. Soc.* **2003**, *125* (2), 541–548. https://doi.org/10.1021/ja027124r.

(78) Perdew, J. P.; Burke, K.; Ernzerhof, M. Generalized Gradient Approximation Made Simple. *Phys. Rev. Lett.* **1996**, *77* (18), 3865–3868. https://doi.org/10.1103/PhysRevLett.77.3865.

(79) Vanderbilt, D. Soft Self-Consistent Pseudopotentials in a Generalized Eigenvalue Formalism. *Phys. Rev. B* **1990**, *41* (11), 7892–7895. https://doi.org/10.1103/PhysRevB.41.7892.

(80) Koelling, D. D.; Harmon, B. N. A Technique for Relativistic Spin-Polarised Calculations. *J. Phys. C Solid State Phys.* **1977**, *10* (16), 3107–3114. https://doi.org/10.1088/0022-3719/10/16/019.

(81) Monkhorst, H. J.; Pack, J. D. Special Points for Brillouin-Zone Integrations. *Phys. Rev. B* **1976**, *13* (12), 5188–5192. https://doi.org/10.1103/PhysRevB.13.5188.

(82) Michaelis, V. K.; Kroeker, S. ^{73}Ge Solid-State NMR of Germanium Oxide Materials: Experimental and Theoretical Studies. *J. Phys. Chem. C* **2010**, *114* (49), 21736–21744. https://doi.org/10.1021/jp1071082.

(83) Sene, S.; Bouchevreau, B.; Martineau, C.; Gervais, C.; Bonhomme, C.; Gaveau, P.; Mauri, F.; Bégu, S.; Mutin, P. H.; Smith, M. E.; Laurencin, D. Structural Study of Calcium Phosphonates: A Combined Synchrotron Powder Diffraction, Solid-State NMR and First-Principle Calculations Approach. *CrystEngComm* **2013**, *15* (43), 8763. https://doi.org/10.1039/c3ce40981c.

(84) Tagg, S. L.; Youngman, R. E.; Zwanziger, J. W. The Structure of Sodium Tellurite Glasses: Sodium Cation Environments from Sodium-23 NMR. *J. Phys. Chem.* **1995**, *99* (14), 5111–5116. https://doi.org/10.1021/j100014a035.

(85) Kravchenko, E. A.; Orlov, V. G.; Shlykov, M. P. Magnetic Properties of Bismuth(III) Oxy Compounds. *Russ. Chem. Rev.* **2006**, *75* (1), 77–93. https://doi.org/10.1070/RC2006v075n01ABEH003596.

(86) Middlemiss, D. S.; Blanc, F.; Pickard, C. J.; Grey, C. P. Solid-State NMR Calculations for Metal Oxides and Gallates: Shielding and Quadrupolar Parameters for Perovskites and Related Phases. *J. Magn. Reson.* **2010**, *204* (1), 1–10. https://doi.org/10.1016/j.jmr.2010.01.004.

(87) Seymour, V. R.; Griffin, J. M.; Griffith, B. E.; Page, S. J.; Iuga, D.; Hanna, J. V.; Smith, M. E. Improved Understanding of Atomic Ordering in $Y_4Si_xAl_{2-x}O_{9-x}N_x$

Materials Using a Combined Solid-State NMR and Computational Approach. *J. Phys. Chem. C* **2020**, *124* (43), 23976–23987. https://doi.org/10.1021/acs.jpcc.0c07281.

(88)   O'Dell, L. A.; Schurko, R. W. QCPMG Using Adiabatic Pulses for Faster Acquisition of Ultra-Wideline NMR Spectra. *Chem. Phys. Lett.* **2008**, *464* (1–3), 97–102. https://doi.org/10.1016/j.cplett.2008.08.095.

(89)   O'Dell, L. A.; Rossini, A. J.; Schurko, R. W. Acquisition of Ultra-Wideline NMR Spectra from Quadrupolar Nuclei by Frequency Stepped WURST–QCPMG. *Chem. Phys. Lett.* **2009**, *468* (4–6), 330–335. https://doi.org/10.1016/j.cplett.2008.12.044.

(90)   O'Dell, L. A. The WURST Kind of Pulses in Solid-State NMR. *Solid State Nucl. Magn. Reson.* **2013**, *55–56*, 28–41. https://doi.org/10.1016/j.ssnmr.2013.10.003.